


Article

A Simplified Microgrid Model for the Validation of Islanded Control Logics

Andrea Bonfiglio *, Massimo Brignone , Marco Invernizzi, Alessandro Labella, Daniele Mestriner and Renato Procopio

DITEN Department of Electrical, Electronic, TLC Engineering and Naval Architecture, University of Genoa, 16145 Genoa, Italy; massimo.brignone@unige.it (M.B.); marco.invernizzi@unige.it (M.I.); alessandrogiuseppe.labella@edu.unige.it (A.L.); daniele.mestriner@edu.unige.it (D.M.); renato.procopio@unige.it (R.P.)

* Correspondence: a.bonfiglio@unige.it; Tel.: +39-010-353-2730

Received: 19 June 2017; Accepted: 30 July 2017; Published: 3 August 2017

Abstract: Microgrids (MGs) may represent a solution in the near future to many problems in the energy and electric world scenarios; such as pollution, high reliability, efficiency and so on. In particular, MGs' capability to work in an islanded configuration represents one of their most interesting features in terms of the improvement of the reliability of the system, the integration of renewable energy sources and the exploitation of the quick response and flexibility of power electronic devices in a stand-alone system. In order to study and validate innovative solutions and control strategies for islanded operation, there is a need to develop models for MG structures that can be reliable and sufficiently simple to be used for the purpose of the design and validation of innovative control systems. This paper proposes a simplified, first harmonic model for a generic structure of MG characterized by its use of only electronic power converter interfaced generation. The main advantages of the proposed method lie in the model's simplicity and its reduced solving time, thanks to the limited number of necessary parameters to describe the system. Moreover, the developed formulation allows the avoidance of specific (and often licensed) software to simulate the system. The performances of the proposed model have been validated by means of a comparative analysis of the results obtained against a more accurate representation of the system performed in the power system CAD—electromagnetic transient and DC (PSCAD—EMTDC) environment, which allows for the representation of each component with a very high level of detail. Such comparison has been performed using the University of Genoa Savona Campus Smart Polygeneration Microgrid testbed facility, due to the availability of all the necessary numerical values.

Keywords: microgrid; distribute control; islanded microgrid; droop control; microgrid simulation; microgrid model; storage characterization

1. Introduction

The development of renewable energy sources (RESs) and of distributed energy resources (DERs), aimed at the reaching of a reduction in greenhouse gas emissions, has led to a massive growth of microgrid (MG) studies and actual realizations [1–3]. The integration of RES is one of the most important and challenging aspects that researchers are facing in order to obtain a stable and reliable operation of the power grid, as the increasing number of wind and photovoltaic power plants is decreasing the inertia of the power system [4–6]. MGs can easily integrate RES into the electric network, guaranteeing an optimized management, both from the economic and the environmental point of view, and a higher level of power quality [7,8]. Moreover, if an MG is capable of working in an islanded configuration and to seamlessly transit from an islanded to grid-connected form, and

vice-versa, this could generate a scenario where the power system is capable of modulating itself in accordance to the need of having a stable asset using MG capabilities to modulate the balance between load and generation. Due to their complexity and the variety of their sources and infrastructures, MGs also represent one of the best environments for the testing of innovative and advanced control and energy management systems. In this framework, the necessity for a reliable model of an MG is essential in order to use it for control system design, the tuning of its parameters and the validation of innovative energy management logics. This goal can be reached, in one way, by representing the MG in an electromagnetic power system simulator (e.g., power system CAD—electromagnetic transient and DC (PSCAD—EMTDC) [9], SPICE (simulation program with integrated circuit emphasis) [10], PLECS (piecewise linear electrical circuit simulation) [11]). The advantage of this approach is that the resulting model is extremely detailed; on the other hand, (i) it requires a lot of time set up the model; (ii) trained users are required and (iii) each simulation becomes very cumbersome from a CPU point of view. It is well known that any model introduces approximations and has a domain of validity. The value of a model is represented by the tradeoff between reliability, accuracy and simplicity: in particular, this last characteristic is very important for the reduction of computational effort and to give the users the possibility to handle the model easily and to have a sensitivity regarding the way variables interact with each other. Indeed, another possible approach is to develop a simplified model that is able to describe all the phenomena that must be taken into account when designing a proper control system suited for a specific MG. Simplified equivalent models are very strong instruments for analyzing MG behavior; an overview on these models is presented in [12,13]. One of the most commonly-used approximations consists of neglecting the voltage drop along the connection (i.e., the so-called single bus bar (SBB) model, according to which generators and loads are positioned at the same bus [14–16]). In other works [17–19], in order to evaluate the power flow easily, voltages are considered equal to one per unit so that it is possible to mismatch current with apparent power. Moreover, in [20] a simplified ordinary differential equations (ODEs) system to evaluate MG behavior is presented; for economic purposes only.

The most relevant part of the bibliography deals with the developing of MG models in the view of energy management systems accounting for longer time horizons (several seconds, hours, days), in order to manage power sharing and the stochastic behavior of loads and renewables [21–24]. The amount of the literature is considerably reduced if one considers islanded microgrids, especially those characterized by no synchronous generators connecting directly to the main AC system. In this configuration, the issue of frequency and voltage control and load sharing is more difficult and cannot rely on the scheme adopted for traditional regulation. For this reason, a simplified way of representing the dynamic behavior of a MG characterized by only power electronic interfaced generation would represent a useful tool to study and test innovative control strategies for islanded MGs.

The present paper aims at developing a simplified model that accounts for all the details typical of a fundamental frequency analysis and is able to handle and to evaluate all the voltage and frequency transients necessary to test a primary regulation scheme. As will be clarified later in the paper, contrary to the SBB approximation, the methodology proposed in this paper does not neglect voltage deviations and/or power losses [16–20,25] and allows one to perform a complete analysis of the evolution of all the electric variables. The proposed approach results in a system of ODEs that can be implemented in any general purpose software, opening the possibility of interfacing it with both traditional MG control systems [26–29] and more advanced ones [30–32] and allowing it to account both for islanded and grid-connected configurations. In other words, the challenge of the proposed model, which represents an optimal trade-off between accuracy and simplicity, is that it can be used as a universal general MG emulator, just like a base brick compatible with many lids, representing the control logics (Figure 1). These lids can be elementary, as droop [27], isochronous [33] and current sharing [34], but also based on complex and advanced optimization and control algorithms (e.g., model predictive control (MPC) [35–37] and feedback linearization (FBL) [38]). In conclusion, the advantages of the proposed model can be summarized as follows:

- (a) Provide a simple but reliable model for islanded MGs, characterized by all the generation interfaced to the AC part of the MG by means of power electronic devices;
- (b) Running the model does not require a dedicated, often licensed, specific software, a relevant time to set up the model and a high computational effort;
- (c) The model is presented as a system of ODE that does not need too many input parameters and can be used to design different controllers and tune their parameters.

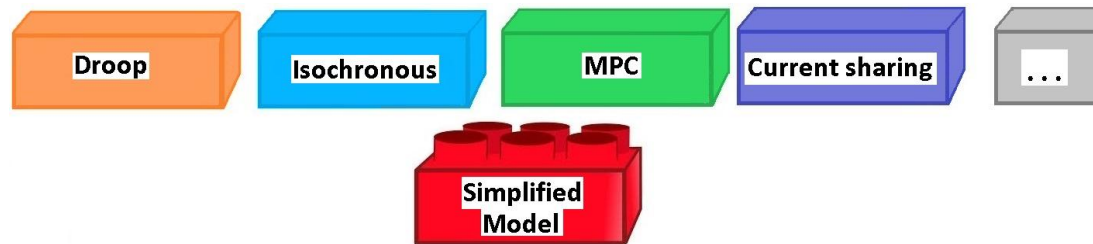


Figure 1. Graphical representation of the proposed concept of defining a simplified model that can be used with various control strategies.

The proposed model has been validated comparing its results with the ones provided by PSCAD—EMTDC on the Smart Polygeneration Microgrid (SPM) of the Savona Campus of Genoa University [39], highlighting a very good agreement between the two simulators.

The paper is organized as follows: Section 2 briefly presents the SPM layout while Section 3 describes its main elements; Section 4 derives the simplified model, highlighting the main assumptions it relies upon. Section 5 recalls the principles of two control strategies, which are used as an example to show the interfacing between the developed power system model and the controller equations. Section 6 presents the power system CAD (PSCAD) environment SPM complete model used to validate the proposed approach and the simulation results. Finally, in Section 7 some conclusions about the work are drawn.

2. The Savona Campus Smart Polygeneration Microgrid

The SPM is a tri-generative, low voltage (LV) MG realized in the Savona Campus of Genoa University, in operation since February 2014. The SPM is an infrastructure realized for demonstrative and research purposes and is intended as a test-bed facility for innovative solutions for MG management and control. In order to achieve this goal, the SPM accounts for various types of generations (tri-generative micro-turbine, photovoltaic and concentrating solar power units), storage devices, electric vehicle charging stations, thermal production units and the campus as an electric and thermal load. The SPM project now represents an important research area for the validation of new algorithms, logics and management strategies to provide and improve innovative solutions to the problem of the integration of DERs and energy storages; fundamental requirements, for example, to the European 20-20-20 calls (Horizon 2020 Programme for Research) [40]. In 2017, a portion of SPM is being tested in an islanded configuration and analyzed in terms of stability and load sharing. This portion is represented in Figure 2 and consists of:

- The public grid connected to a switchgear (SG) Q1;
- Three photovoltaic (PV) units connected through a unique cable to the SG Q1, namely PV1;
- One PV unit (with its inverter and transformer) connected to SG Q2, namely PV2;
- The storage unit produced by FIAMM (with its DC/DC converter, inverter and transformer) connected to SG Q2;
- Resistive-inductive loads connected to SG Q2.

The sources, ratings, and the main data of the network components are reported in Table 1.

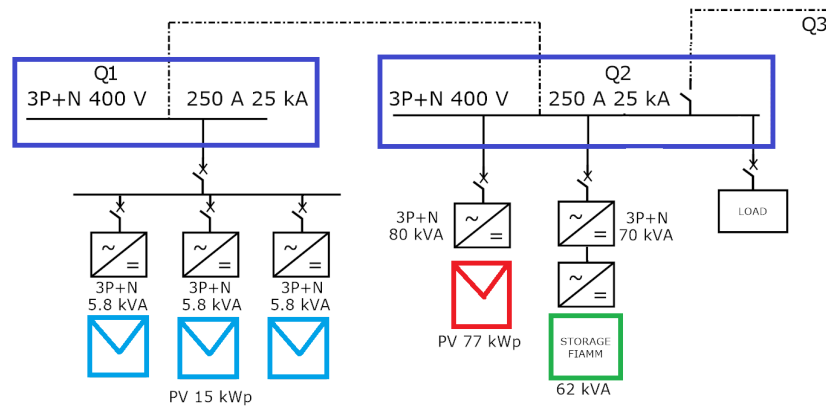


Figure 2. Smart Polygeneration Microgrid (SPM) portion used to create the island.

Table 1. Sources data.

	Photovoltaic (PV) 1	PV 2	Storage	Load
Rated Power	3×5 kWp	77 kWp	62 kW	
Cable resistance to Q2	157.2 mΩ	20.8 mΩ	43.5 mΩ	181 mΩ
Cable inductance to Q2	3023.7 μH	14.15 μH	12.42 μH	14.59 μH

Moreover, both PV2 and the storage have a transformer, whose rated values are 80 kVA, 6%, 200/400 V and 70 kVA, 4%, 400/400 V respectively.

3. MG Sources and Main Elements

In the present section, a mathematical modeling of the SPM components involved in the islanded portion is presented.

3.1. PV Units Model

The PV modules are modeled as DC dipoles whose voltage–current characteristic curve (dependent on the irradiance α in W/m^2 , the temperature T in $^{\circ}\text{C}$ and the V voltage expressed in V) in the I–V plane is described as follows [41]:

$$I(\alpha, T, V) = \frac{\alpha}{1000} I_{SC} \tau_i(T) \left[\frac{1 - e^{\frac{V}{b(1 + \frac{V_{MAX} - V_{MIN}}{V_{MAX}} \cdot \frac{\alpha - \alpha_{MAX}}{\alpha_{MAX} - \alpha_{MIN}}) \cdot (V_{MAX} + \tau_V(T))}} - \frac{1}{b}}}{1 - e^{-\frac{1}{b}}} \right] \quad (1)$$

where the meaning of symbols and their values are reported in Table 2. The number p of parallel modules and s of series modules is: $p = 3$ and $s = 22$ for PV1 and $p = 14$ and $s = 24$ for PV2.

Table 2. PV Module parameters.

PV Module Parameters		
Short circuit current in Standard Test Conditions (STC)	I_{SC}	8.75 A
Rated external temperature	T_N	25 $^{\circ}\text{C}$
Temperature coeff. of the short circuit current	T_{CI}	0.06
Temperature coeff. of the open module voltage	T_{CV}	−0.31
Minimum solar radiation to supply energy	α_{MIN}	0.2 kW/m^2
Maximum solar radiation to supply energy	α_{MAX}	1 kW/m^2
Open voltage module at α_{MIN}	V_{MIN}	35 V
Open voltage module at α_{MAX}	V_{MAX}	37.11 V
Maximum power point voltage in STC	V_{MPP}	29.7 V
Maximum power in STC	P_{MPP}	240 W

3.2. Electric Storage Model

The electric storage system is a FIAMM SoNick battery (Zebra), with a rated capacity of 141 kWh, 228 Ah of nominal current capacity (NCC), a rated power of 62 kW when supplying and 30 kW when absorbing. It is structured in $N_m = 6$ modules in parallel, each one composed by the series of $N_c = 240$ cells [42]. The storage is represented by a non-ideal DC voltage generator, where the produced voltage V is a function of its state of charge (SOC) [43], its internal resistance R_{int} and the current I injected by the storage, according to the following equation:

$$V \equiv V(SOC, I) = E(SOC) - IR_{int} \quad (2)$$

where the internal voltage (E) is an unknown function of the SOC, to be deduced from measured data. The model proposed in (2) is justified observing Figure 3, where it can be noticed that discharging the battery at different (constant) currents results in a rigid translation of the curve. Under this assumption, for a fixed value of the SOC, the voltage V depends proportionally on the current. In terms of an electric equivalent, if there is a linear relationship between voltage and current, there is an internal resistance whose value can be estimated by simply knowing two voltage-current couples.

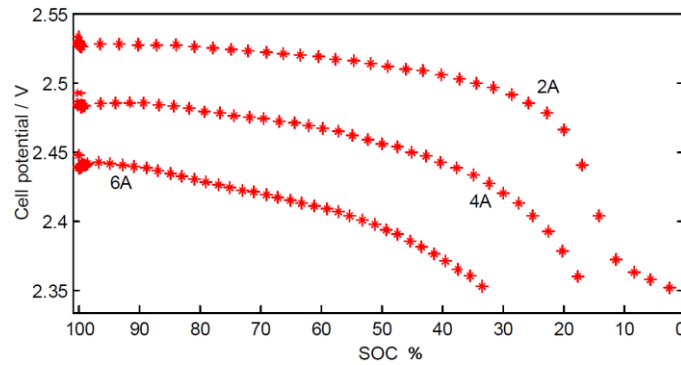


Figure 3. Voltage–state of charge (V/SOC) cell characteristics [43]

For each current I , a set of N measurements is available in Figure 3, formally encoded in the following:

$$\left\{ \left(SOC_k, V_{k,I_p} \right) : k = 1, \dots, N \text{ and } p = 1, \dots, N_I \right\} \quad (3)$$

where, for our measurements, $N_I = 3$ and $I_1 = 2$ A, $I_2 = 4$ A and $I_3 = 6$ A. The cell resistance value can be calculated as the following average:

$$R_{cell} = \frac{1}{N_I N} \sum_{k=1}^N \left[\sum_{\substack{p, q = 1 \\ I_q > I_p}}^{N_I} \left(\frac{V_{k,I_p} - V_{k,I_q}}{I_q - I_p} \right) \right] \quad (4)$$

which allows us to find that $R_{cell} = 0.028 \Omega$. As a consequence, the pairs $(SOC_k, E_{cell,k})$ can be obtained as follows:

$$E_{cell,k} = V_{k,I_1} + R_{cell} \cdot I_1 \quad (5)$$

Finally the possible analytical expression for the link between the internal voltage and the SOC can be obtained fitting the pairs $(SOC_k, E_{cell,k})$ with the following polynomial formula:

$$E_{cell} = \sum_{i=0}^6 a_i \cdot SOC^i \quad (6)$$

where the coefficients a_i have been found with a least-square method aimed at minimizing the difference between the polynomial output and the measured sequence $E_{cell,k}$. The numerical values of the coefficients are reported in Table 3 and the resulting curve is depicted in Figure 4.

Table 3. Polynomial coefficients

[A]	a_6	a_5	a_4	a_3	a_2	a_1	a_0
0 [A]	1.6×10^{-11}	-4×10^{-9}	6×10^{-7}	-3.3×10^{-5}	7.5×10^{-4}	5.2×10^{-4}	2.42

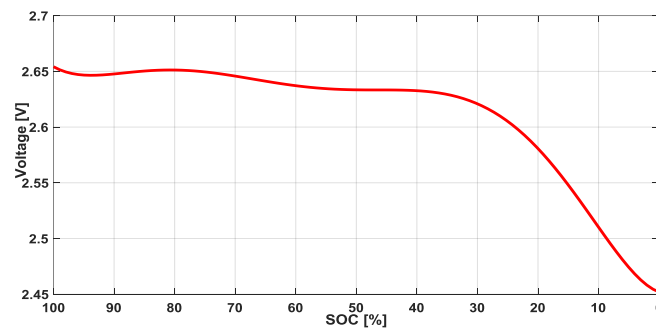


Figure 4. Voltage against SOC cell characteristic

Then, the results for the maximum voltage of a single cell are:

$$E_{cell}(SOC = 100\%) = 2.66 \text{ V} \quad (7)$$

therefore, the maximum voltage of the overall storage is:

$$E(SOC = 100\%) = E_{cell}(SOC = 100\%) \cdot N_c = 2.66 \text{ V} \cdot 240 = 640 \text{ V} \quad (8)$$

and the internal resistance is:

$$R_{int} = \frac{R_{cell} \cdot N_c}{N_m} = \frac{R_{cell} \cdot 240}{6} = 1.12 \Omega \quad (9)$$

The dependence of the voltage on the temperature is neglected according to Zebra features [44]. Often, and therefore also in this MG, a DC/DC bidirectional converter is interposed between the storage and its inverter (this will be discussed in detailed in the following).

3.3. Inverter Model

The aim of the inverter is to couple the DC sources to the AC grid correctly. Each inverter is modeled by the mean-values input/output relation, thus:

$$\dot{V}_{AC} = \frac{m V_{DC} e^{j\delta}}{2\sqrt{2}} \quad (10)$$

where \dot{V}_{AC} is voltage phasor, m is the modulation index, V_{DC} is the voltage at DC terminals, j , as usual, is the imaginary unit, and δ is the angle of the phasor.

Each inverter presents a filter posed at its AC terminals in order to attenuate high frequency harmonics and a capacitor of 2.5 μF at the DC terminals in order to stabilize the voltage. Figure 5 and Table 4 present the configuration and the parameters of the filter.

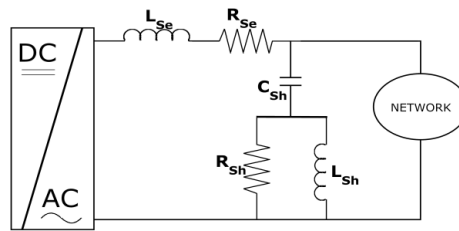


Figure 5. Inverter AC filter configuration.

Table 4. AC filter parameters.

L_{se}	R_{se}	L_{sh}	C_{sh}	R_{sh}
1 mH	0.314 m Ω	0.0166 mH	1 μF	2.61 k Ω

3.4. DC/DC Converter Model

In order to allow for the proper operation of the inverter, it is necessary to keep its DC voltage as constant as possible. Thanks to the MPPT (maximum power point tracker) algorithm, PV inverters are controlled in a way that keep the DC voltage almost constant, as the MPP (maximum power point) voltages do not vary by very much [45]. The storage inverters, on the other hand, are characterized by a sensitive variation of the voltage on the battery; thus, they need a dedicated control of the voltage obtained by the insertion of a DC/DC bi-directional (buck-boost) chopper. The DC/DC converter has the structure depicted in Figure 6 [46].

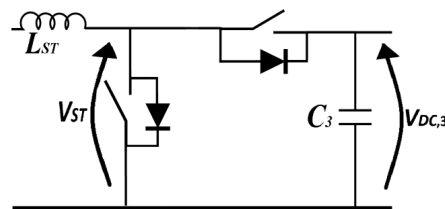


Figure 6. DC/DC converter circuit layout.

The well-known chopper input/output relationship [46] is given by:

$$V_{DC,3} = K_{ST} V_{ST} \quad (11)$$

being $V_{DC,3}$ and V_{ST} the DC/DC output (inverter side) and input (battery side) voltages respectively, while K_{ST} is related to the switch duty cycles D_1 (boost) and D_2 (buck) according to the following:

$$K_{ST} = \begin{cases} \frac{1}{1-D_1} & P_{ST} \geq 0 \\ \frac{1}{D_2} & P_{ST} < 0 \end{cases} \quad (12)$$

being P_{ST} the power injected by the storage into the network. Moreover, a filter consisting of a series inductor and a shunt capacitor have been inserted, whose values are 1 mH and 0.5 mF respectively.

4. The Simplified Model

The aim of this work is to find an approximate model able to adequately represent both the transient and the steady state of any MG, after a contingency. To do this, the following simplifications are introduced:

- Each input/output power electronic converter relationship neglects the presence of the higher order harmonics;
- The shunt sections of the inverter AC filters are neglected for simplicity (indeed it can be noted from Table 3 that the shunt filter impedance at the fundamental frequency is more than 3 k Ω). If one considered this, it would imply only an enlargement of the network admittance matrix Y without changing the model structure;
- The AC-side portion of the MG (as well as the inverter filter) is supposed to be at a steady state (assuming that both the angular frequency of the sources and their voltage amplitude can vary), while all the DC dynamics are accounted;
- The loads are described with a constant impedance model. Consequently, as typical in RMS transients, they are inserted in the network model, giving rise to the so-called extended admittance matrix Y_E [47].

Thus, in the case of the SPM, the portion described in Figure 2 collapses in the one shown in Figure 7. As will be clear in writing the equations, it is apparent that the description of the AC grid with the extended admittance matrix allows for a coupling of the source dynamics in a simple but effective way.

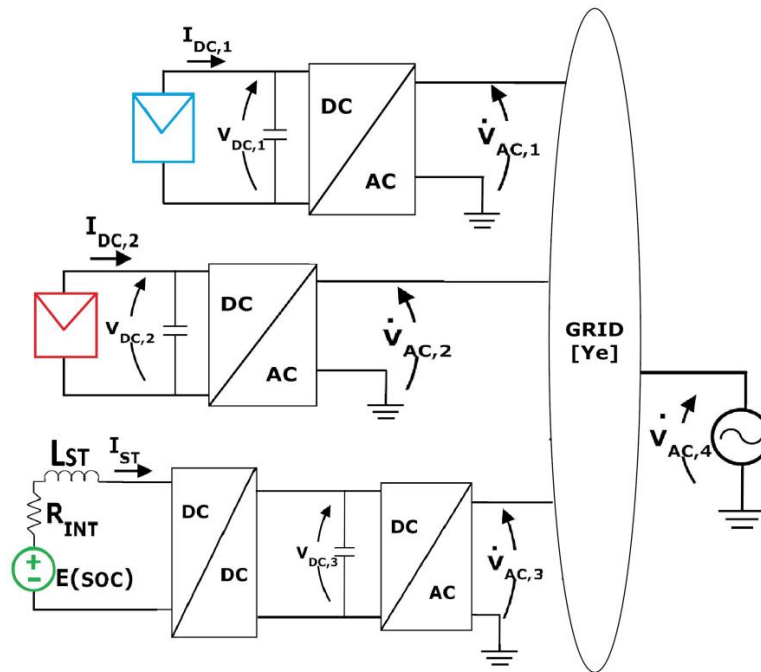


Figure 7. Simplified model of the islanded portion of the SPM.

The first assumption allows us to write that [46]:

$$\dot{V}_{AC,k}(t) = \frac{m_k(t)}{2\sqrt{2}} V_{DC,k}(t) e^{j\delta_k(t)} \quad k = 1, 2, 3 \quad (13)$$

where j , as usual, is the imaginary unit, and, for the k -th source, m_k is the modulation index (in accordance to its linear meaning [46], it lies in the range (0, 1.15)) and δ_k is the angle such that:

$$\delta_k(t) = \psi_k(t) + \varphi_k(t) \quad (14)$$

where

$$\frac{d\psi_k(t)}{dt} = \omega_k(t) \quad (15)$$

while ω_k and φ_k are the angular frequency and the phase of the k -th source, respectively. The main network is an independent voltage source, whose phasor is given by:

$$\dot{V}_{AC,4} = V_{AC,4} e^{j\delta_4} \quad (16)$$

Thus, the active power injected by the k -th source ($k = 1, 2, 3$) is given by:

$$\begin{aligned} P_{AC,k}(t) &= 3 \operatorname{Re} \left\{ \dot{V}_{AC,k} \dot{I}_{AC,k}^* \right\} = 3 \operatorname{Re} \left\{ \dot{V}_{AC,k} \sum_{i=1}^4 \left(\dot{Y}_{E,ki}^* \dot{V}_{AC,i} \right) \right\} \\ &= 3 \frac{m_k(t) V_{DC,k}(t)}{8} \sum_{i=1}^3 \left\{ m_i(t) V_{DC,i}(t) [\cos(\delta_k(t) - \delta_i(t)) G_{ki} + \sin(\delta_k(t) - \delta_i(t)) B_{ki}] \right\} \\ &\quad + 3 \frac{m_k(t) V_{DC,k}(t)}{2\sqrt{2}} \left\{ V_{AC,4} [\cos(\delta_k(t) - \delta_4(t)) G_{k4} + \sin(\delta_k(t) - \delta_4(t)) B_{k4}] \right\} \end{aligned} \quad (17)$$

where $Y_{E,ki} = G_{ki} + jB_{ki}$ is the (k, i) element of the extended admittance matrix. As stated before, Equation (17) shows the strong coupling of the sources through Y_E . Moreover, for each PV capacitor, the power balance can be written as:

$$C_k V_{DC,k} \frac{dV_{DC,k}}{dt} = V_{DC,k} I_{PV,k}(V_{DC,k}) - 3 \operatorname{Re} \left\{ \dot{V}_{AC,k} \dot{I}_{AC,k}^* \right\} \quad k = 1, 2 \quad (18)$$

while the storage capacitor power balance results in:

$$C_3 V_{DC,3} \frac{dV_{DC,3}}{dt} = \frac{V_{DC,3} I_{ST}}{K_{ST}} - 3 \operatorname{Re} \left\{ \dot{V}_{AC,3} \dot{I}_{AC,3}^* \right\} \quad (19)$$

Furthermore, the storage device current dynamic equations are:

$$L_{ST} \frac{dI_{ST}}{dt} = E(\operatorname{SOC}) - R_{int} I_{ST} - \frac{V_{DC,3}}{K_{ST}} \quad (20)$$

$$\frac{d\operatorname{SOC}}{dt} = \frac{-I_{ST}}{NCC} \quad (21)$$

L_{ST} and R_{int} appear in Figure 7.

Inserting (14) into (17), then (17) into (18) and (19), one finally gets the system of ordinary differential Equations (15) and (18)–(21), which completely describes the DC dynamics, and so the complete dynamics of the MG under the aforementioned assumptions. A differential equations (ODE) system can be written as:

$$\dot{\mathbf{x}} = \mathbf{f}(\mathbf{x}, \mathbf{U}) \quad (22)$$

where \mathbf{f} collects (15) and (18)–(21), while the vectors \mathbf{x} and \mathbf{U} are given by:

$$\begin{aligned} \mathbf{x} &= \left[V_{DC,1} \quad V_{DC,2} \quad V_{DC,3} \quad I_{ST} \quad \operatorname{SOC} \quad \psi_1 \quad \psi_2 \quad \psi_3 \right]^T \\ \mathbf{U} &= \left[m_1 \quad m_2 \quad m_3 \quad \omega_1 \quad \omega_2 \quad \omega_3 \quad \varphi_1 \quad \varphi_2 \quad \varphi_3 \right]^T \end{aligned} \quad (23)$$

The initial equilibrium point can be obtained by solving the non-linear algebraic system, obtained by zeroing all the time derivatives in (22).

Starting from an assigned equilibrium point, a structure perturbation (encoded in a variation in one or more elements of the extended admittance matrix) causes the dynamics. It is useful to underline

that, in order to exclude a source from the analysed grid, it is sufficient to cancel the related admittances, highlighting the flexibility of the proposed approach to be applied at different MG structures. It is important to highlight that U is the input vector used to create the modulating signal of the PWM (pulse-width modulation) to control the AC voltage of each inverter: amplitude (m), frequency (ω) and phase (φ).

In conclusion, a step by step synopsis could be useful to summarize the whole procedure:

1. Define the MG topology, parameters (rated data of cables, transformers, sources etc.) and admittance matrix;
2. Define the sources and their characteristic (power–irradiance for PV, power–wind velocity for wind generator, V-SOC for chemical storage etc.);
3. Define the all the state variables and write the resulting ODEs;
4. Define an equilibrium point of the system zeroing all of the time derivatives;
5. Define a contingency;
6. Solve the resulting ODE system and get the involved variable dynamics.

5. Controllers

One of the aims of the paper is to show that the developed model can be adopted to design suitable MG controllers, set up their parameters and test their performances. To do this, in the present section, after a brief overview of the control system for the DC/DC converter (Section 5.1), two control examples are described; namely, the droop-based control (quickly recalled in Section 5.2) and the isochronous control (summarized in Section 5.3).

5.1. DC/DC Converter Controller

The DC/DC converter control logic is explained by (24) and (25), where the sign of the power produced by the storage in AC side (P_{ST}) activates either the buck or the boost level control. Both of them consist of PI (proportional integral) regulators that implement the following equations:

$$\begin{aligned} D_1 &= K_{PBOOST} \left(V_{DC,3,rif} - V_{DC,3} \right) + \chi_1 \\ D_2 &= -K_{PBUCK} \left(V_{DC,3,rif} - V_{DC,3} \right) + \chi_2 \end{aligned} \quad (24)$$

being

$$\begin{aligned} \dot{\chi}_1 &= \frac{(V_{DC,3,rif} - V_{DC,3})}{T_{BOOST}} \\ \dot{\chi}_2 &= -\frac{(V_{DC,3,rif} - V_{DC,3})}{T_{BUCK}} \end{aligned} \quad (25)$$

Thus, χ_1 and χ_2 represent the state of the two different PI controllers.

The chosen proportional gains and integral time constants appear in Table 5. The whole system being strongly non-linear, the usual tuning techniques lack validity; thus, here and in the following the PI parameters are chosen in a heuristic way to get the best performance in terms of system stability and transient/steady state behavior.

Table 5. DC/DC PI Parameters.

	Proportional Gain	Integral Time Constant
Boost	$K_{P_BOOST} = 1.438 \times 10^{-4}$	$T_{BOOST} = 8.749$ (s)
Buck	$K_{P_BUCK} = 1.667 \times 10^{-4}$	$T_{BUCK} = 10$ (s)

5.2. Droop Control

The droop control, first proposed by M. C. Chandorkar in 1993 [27], is a technique that allows the sharing the load power among different sources without the need for any communication device. Details on the method can be found in [15,48,49]; here, the main controller equations are reported and then connected to those describing the power system model.

$$\omega_k = \omega_0 + m_{Dk}(P_{AC,k} - P_{AC,k0}) \quad (26)$$

$$V_k = V_{k0} + n_{Dk}(Q_k - Q_{k0}) \quad (27)$$

where m_{Dk} (n_{Dk}) is a negative coefficient that represents the slope of the P- ω (Q-V) droop characteristic of the k -th inverter; $P_{AC,k0}$ (Q_{k0}) is the reference of the active (reactive) power of the machine; $P_{AC,k}$ (Q_k) is the actual active (reactive) power produced by the k -th source; V_{k0} is the k -th inverter AC side voltage (reference) and ω_0 is the rated angular frequency of the MG. In order to ensure a proper load sharing among the sources, m_{Dk} and n_{Dk} are chosen according to the rated active and reactive power (P_{iN} and Q_{iN}) respectively [27,28] thus:

$$\begin{cases} m_{D1}P_{1N} = m_{D2}P_{2N} = \dots = m_{Dk}P_{kN} \\ n_{D1}Q_{1N} = n_{D2}Q_{2N} \dots = n_{Dk}Q_{kN} \end{cases} \quad (28)$$

Equation (28) states that, whatever the number of sources in the MG, just one droop coefficient for the active power channel, and only one for the reactive one, can be chosen independently. Inserting (17) into (26), one has:

$$\omega_k - \omega_0 = m_{Dk} \left[3 \frac{m_k V_{DC,k}}{8} \left(\sum_{i=1}^3 m_i V_{DC,i} \{ \cos(\delta_k \delta_i) G_{ki} + \sin(\delta_k - \delta_i) B_{ki} \} + \right. \right. \\ \left. \left. + 2\sqrt{2} V_{AC,4} [\cos(\delta_k - \delta_4) G_{k4} + \sin(\delta_k - \delta_4) B_{k4}] \right) - P_{AC,k0} \right] \quad (29)$$

$k = 1 \dots 3$

As pointed out in [27], the droop control does not act on the initial phase φ_k , which is locked to its initial value. So, inserting (29) into (18), one has:

$$\frac{d\delta_k}{dt} = m_{Dk} \left[3 \frac{m_k V_{DC,k}}{8} \left(\sum_{i=1}^3 m_i V_{DC,i} \{ \cos(\delta_k - \delta_i) G_{ki} + \sin(\delta_k - \delta_i) B_{ki} \} + \right. \right. \\ \left. \left. + 2\sqrt{2} V_{AC,4} [\cos(\delta_k - \delta_4) G_{k4} + \sin(\delta_k - \delta_4) B_{k4}] \right) - P_{AC,k0} \right] \quad (30)$$

$k = 1 \dots 3$

Moreover, combining the k -th inverter reactive power expression with (27), one has:

$$V_{k0} - \frac{m_k V_{DC,k}}{2\sqrt{2}} + n_{Dk} \left[\left(3 \frac{m_k V_{DC,k}}{8} \left(\sum_{i=1}^3 \{ m_i V_{DC,i} [\sin(\delta_k - \delta_i) G_{ki} - \cos(\delta_k - \delta_i) B_{ki}] \} + \right. \right. \right. \\ \left. \left. + 2\sqrt{2} V_{AC,4} [\sin(\delta_k - \delta_4) G_{k4} - \cos(\delta_k - \delta_4) B_{k4}] \right) \right) - Q_{k0} \right] = 0 \quad (31)$$

$k = 1 \dots 3$

which produces the following differential-algebraic equations (DAEs) system:

$$\begin{cases} \dot{x}_D = f_D(x_D, \mathbf{U}) \\ 0 = g_D(x_D, \mathbf{U}) \end{cases} \quad (32)$$

in which the vector of the states \mathbf{X}_D is given by:

$$\mathbf{x}_D = [V_{DC,1} \ V_{DC,2} \ V_{DC,3} \ I_{ST} \ SOC \ \delta_1 \ \delta_2 \ \delta_3 \ \chi_1 \ \chi_2]^T \quad (33)$$

and U is the vector that contains V_{k0} and ω_0 . Figure 8 shows the strong relation between the control logic and the simplified model, as the input of the power system are the output of the control system and the input of the control systems are the measured and feed-backed power system results.

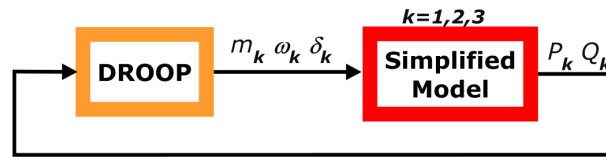


Figure 8. Block scheme droop strategy.

The function f_D appearing in (32) consists of (18)–(21), (25) and (30), having expressed K_{ST} as a function of the state variables using (12) and (24), while g_D collects (31).

5.3. Isochronous (Master/Slave) Control

The main goal of the isochronous control is to allow the PV sources (slaves) to supply their maximum power [33,50,51], controlling them in the so-called PQ (active and reactive power) control mode [29]. In this way, each load variation will be handled completely by the storage system that acts as a master.

Therefore, one controls the storage system such that it acts as a fixed voltage source, while the PV units are managed by two PI controllers. One receives, as an input, the DC voltage error and produces the phase angle δ_k as an output of the modulating signals for the PV inverter, while the other processes the reactive power error in order to provide the PWM logic with a suitable modulating index request m_k (see [52] for details). It should be noted that the isochronous logic does not act on the angular frequencies ω_k , which remain locked in to their rated value. The controllers structure is specified in (34) and (35), while their parameters appear in Table 6.

$$\left. \begin{aligned} \dot{\eta}_{1,k} &= \left(V_{DC,k} - V_{DC,rifk} \right) \frac{1}{T_{phase}} \\ \dot{\eta}_{2,k} &= \left(Q_{rif,k} - Q_k \right) \frac{1}{T_{mod_index}} \end{aligned} \right\} \quad k = 1, 2 \quad (34)$$

$$\left. \begin{aligned} \varphi_k &= K_{P,phase} \cdot (V_{DC,k} - V_{DC,rifk}) + \eta_{1,k} \\ m_k &= K_{P,mod_index} \cdot (Q_{rif,k} - Q_k) + \eta_{2,k} \end{aligned} \right\} \quad k = 1, 2 \quad (35)$$

Table 6. PVs inverter PI Parameters.

	Proportional Gain	Integral Time Constant
phase	$K_{P,phase} = 5 \times 10^{-4}$	$T_{phase} = 10$ (s)
mod_index	$K_{P,mod_index} = 2 \times 10^{-6}$	$T_{mod_index} = 2.5 \cdot 10^3$ (s)

The master/slave control produces the following ODE system:

$$\dot{x}_I = f_I(x_I, U) \quad (36)$$

in which the vector of the states X is given by:

$$X_I = [V_{DC,1} \ V_{DC,2} \ V_{DC,3} \ I_{ST} \ SOC \ \psi_1 \ \psi_2 \ \psi_3 \ \chi_1 \ \chi_2 \ \eta_{1,1} \ \eta_{1,2} \ \eta_{2,1} \ \eta_{2,2}]^T \quad (37)$$

the input vector U contains the reference signals for the PV active and reactive power production and f_I collects (18)–(22), (25) and (34). Figure 9 shows the relation between the control logic and the simplified model.

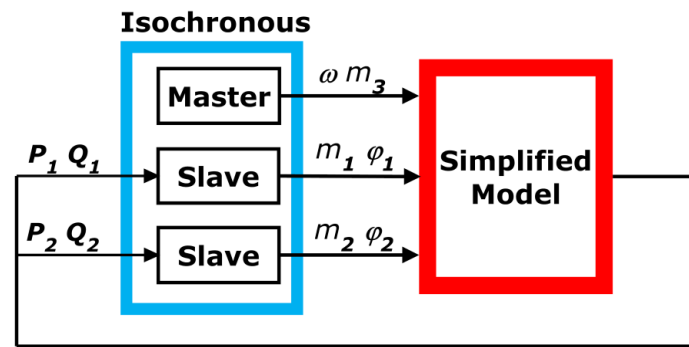


Figure 9. Block scheme isochronous strategy.

6. Simulations

In order to validate the proposed simplified approach, a complete model of the islanded section of the SPM has been set up in the PSCAD-EMTDC environment that allows us to represent all the devices with a high degree of detail. In particular, all the inverters are built with a total controlled bridge of a not-ideal IGBT (insulated gate bipolar transistor), modulated with a PWM technique and equipped with AC filters whose topology appears in Figure 5 using the parameters available in Table 3 [53], considering both the series and the shunt parts. Moreover, the DC/DC converter is an inverter branch modulated through a comparison between a triangle carrier and a reference constant signal [46]. Thus, the whole harmonic spectrum is accounted both at the DC side and at the AC one, contrary to what is done in the simplified model. Finally, the sources are implemented with the same equations used in the simplified model, while the whole infrastructure, being modelled in an electromagnetic environment, accounts both for AC and DC dynamics. A PSCAD view of the complete model is shown in Figure 10.

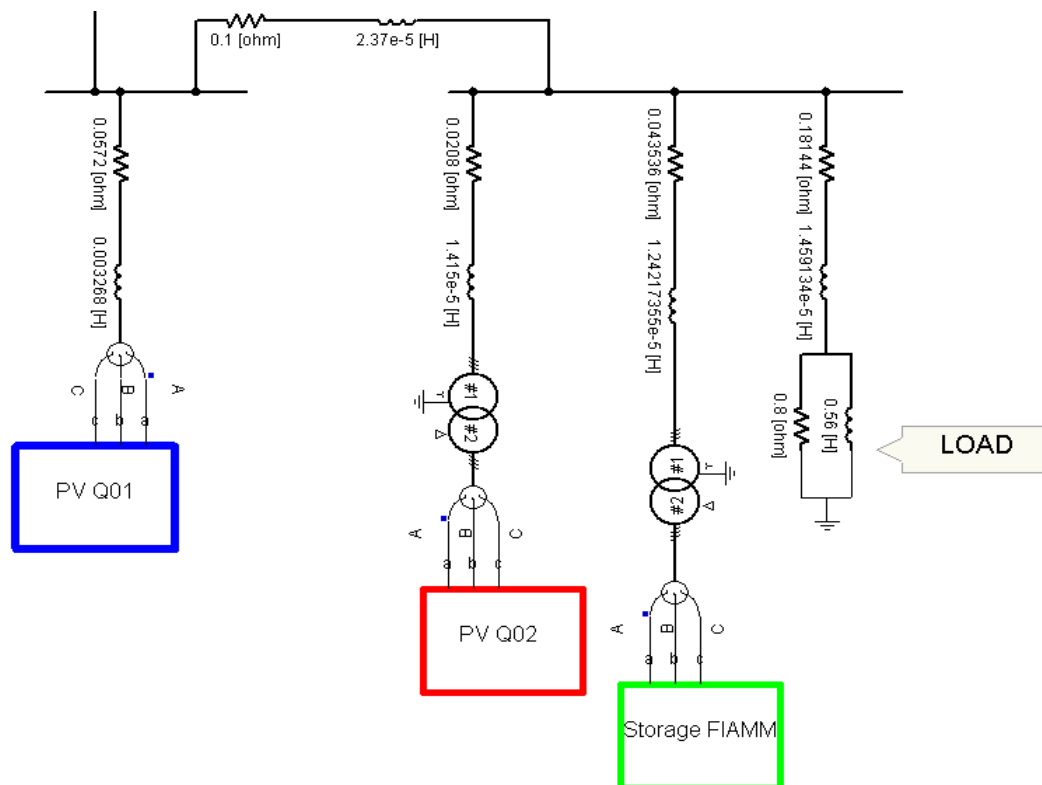


Figure 10. PSCAD model overview

Two groups of simulations will be presented with two main aims:

1. Validating the developed simplified model comparing its results with the ones provided by the complete model implemented in PSCAD-EMTDC;
2. Assessing the possibility of interfacing the developed power system model with different controller structures. This will be done considering the two control logics summarized in the previous sections (droop and isochronous).

6.1. Droop Control Simulations

In the following paragraphs, two simulations will be presented; the first one (S1) is characterized by a step decrease in the load resistance with a consequent increase in its active power request, while, in the second one (S2), the load resistance increases resulting in a decrease in its active power absorption. The values of the droop coefficients chosen for both simulations are reported in Table 7.

Table 7. Droop parameters.

	PV1	PV2	Storage
P_n	15 kW	77 kW	62 kW
m	-1.000×10^{-4} rad/sW	-0.187×10^{-4} rad/sW	-0.242×10^{-4} rad/sW
Q_n	7.265 kVAr	38.746 kVAr	30.03 kVAr
n	-1.000×10^{-4} V/VAr	-0.187×10^{-4} V/VAr	-0.242×10^{-4} V/VAr

6.1.1. Active Power Increasing Simulation (S1)

The initial working point is described in Table 8. The contingency occurs at 0.1 s and consists of a step change in the load resistance from 3Ω to 1.85Ω (corresponding about to 53 and 86 kW respectively), assuming that both the PV panels temperature and the solar irradiance are constant for the whole simulation.

Table 8. S1—Initial states.

PV1	PV2	Storage	DC/DC Converter
$V_{DC,1} = 783.8$ V	$V_{DC,2} = 854.8$ V	$V_{DC,3} = 750.0$ V $I_{ST} = 6.4$ (A) SOC = 80%	$\chi_1 = 0.153$ $\chi_2 = 0.847$
$\psi_1 = 0.0524$ rad $\varphi_1 = 0$	$\psi_2 = 0.0524$ rad $\varphi_2 = 0$	$\psi_3 = 0$ rad $\varphi_3 = 0$	

As shown in Figure 11, the active power surplus is shared among the three sources, which all increase their production. From the comparison standpoint, it can be observed that the steady-state value is well captured by the simplified model, while some differences appear in the transient behavior.

In particular, the dynamics predicted by the proposed approach are much faster than the PSCAD ones; this is due to the fact that one of the main assumptions supporting the developed model supposes the AC portion of the network to be at steady state. Moreover, as demonstrated in [28], the sources' frequencies reach the same steady state value (see Figure 12). This allows the quantification of the active power sharing and the steady-state frequency deviation, equal to -0.045 Hz. From the comparison point of view, the same considerations can be made as in the previous figures concerning the ability of the simplified model to effectively predict the steady-state value with a much faster dynamic.

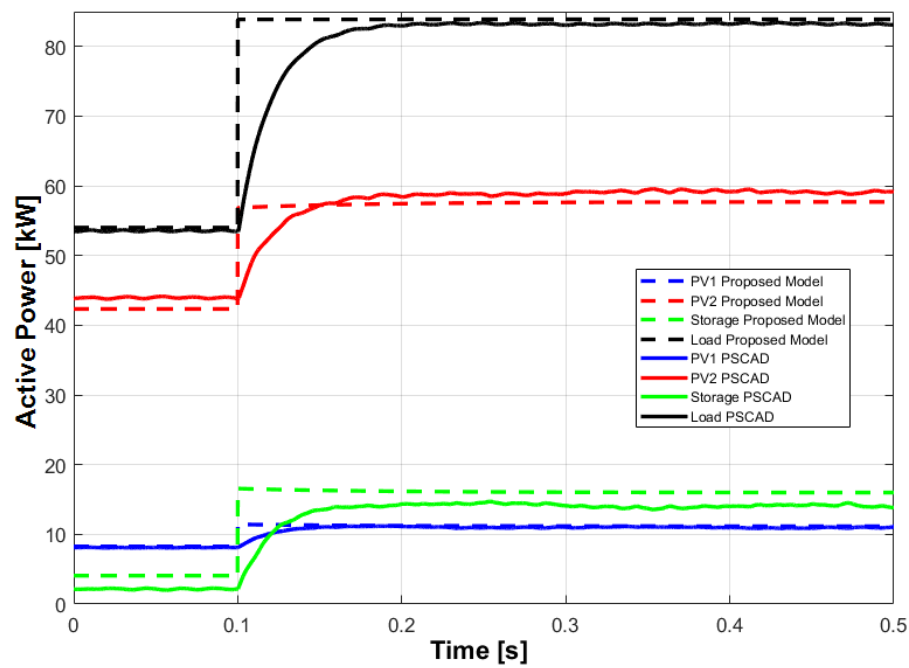


Figure 11. Active power time profile for load increasing scenario; the solid lines refers to PSCAD model while dashed ones refer to the proposed approach.

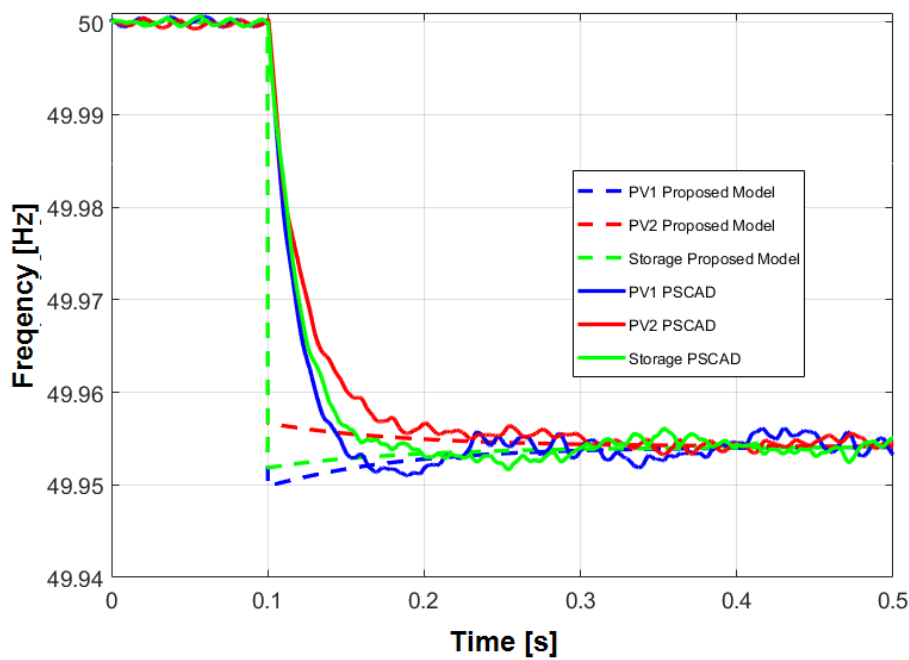


Figure 12. Frequencies output time profile for the load increasing scenario; the solid lines refer to PSCAD model while dashed ones refer to the proposed approach.

As far as the state variables are concerned, Figures 13 and 14 highlight that, both in the transient and in the steady-state, the developed approach shows an excellent agreement with the PSCAD simulations.

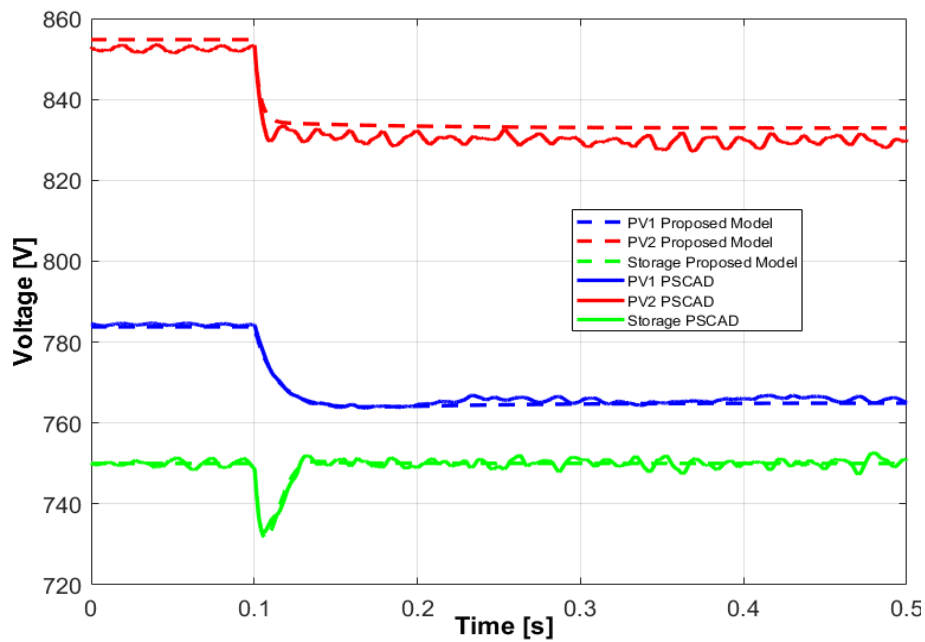


Figure 13. DC capacitor voltage time profile for the load increasing scenario; the solid lines refer to PSCAD model while dashed ones refer to the proposed approach.

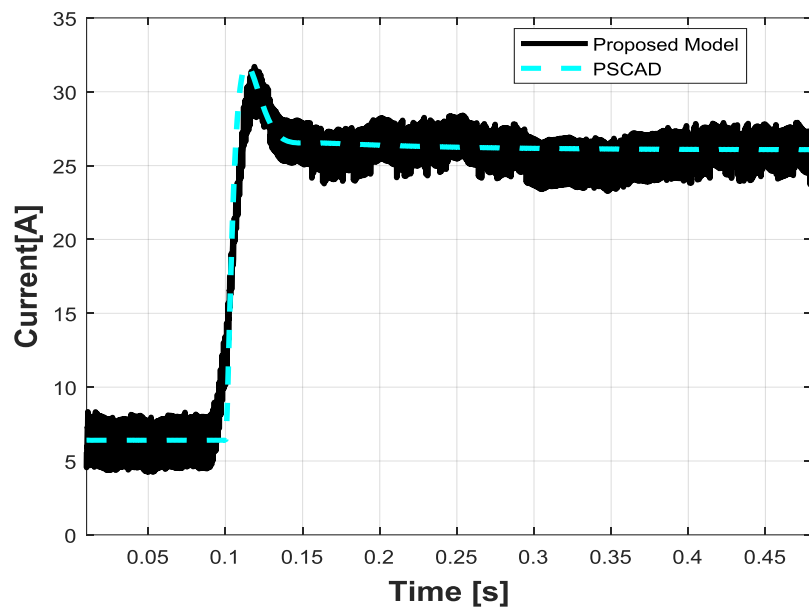


Figure 14. L_{ST} current profile for the load increasing scenario; the solid lines refer to PSCAD model while dashed ones refer to the proposed approach.

Moreover, it can be noted that the increase of the load active power claims for the injection of a higher amount of current by the storage; firstly, this current is supplied by the DC link storage capacitor, which causes a voltage dip of about 0.04 s. Finally, due to the fact that the initial PVs' voltages are over the V_{MPP} (653.4 V and 712.8 V respectively), when the droop control requires the PVs to inject a higher amount of power, the DC voltages decrease.

Finally, Figure 15 plots the Q2 voltage amplitude according to the simplified model and to the PSCAD simulation; again, it is possible observing the quite good agreement characterized by an error smaller than 0.5%.

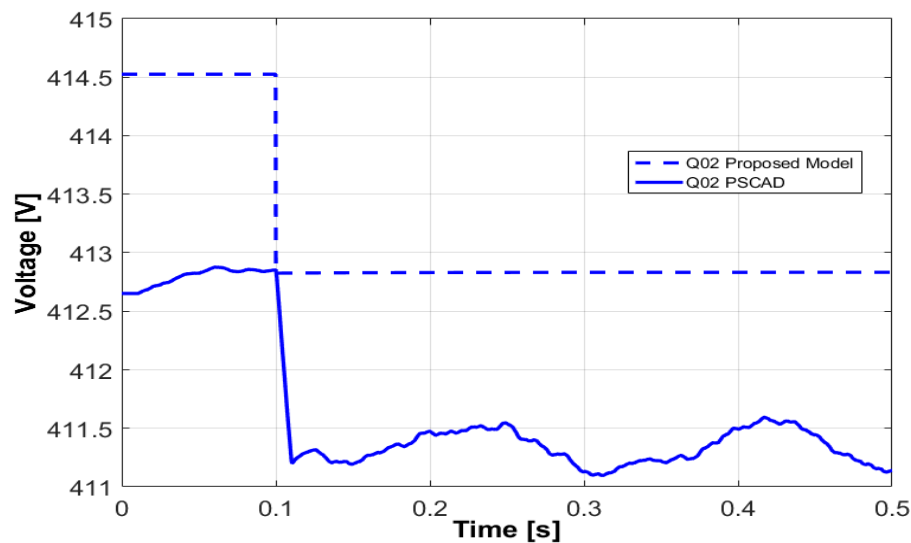


Figure 15. Q2 bus voltage time profile for the load increasing scenario; the solid lines refer to PSCAD model while dashed ones refer to the proposed approach.

6.1.2. Active Power Decreasing Simulation (S2)

The initial point of the active power decreasing simulation is the same as that used for the active power increasing test case (see Table 8). The contingency occurs at 0.1 s and consists of a step change in the load resistance from 3Ω to 10Ω (corresponding to 53 and 16 kW respectively), Figure 16 shows the active power behavior, highlighting a good agreement between the two approaches, with some small deviations in the steady-state values of the power provided by the storage and the bigger PV unit. As far as the transient behavior is concerned, the same considerations as before can be made. The active power sharing among the sources and the final value of the system frequency can be appreciated examining Figure 17 in which a frequency deviation of +0.056 Hz occurs.

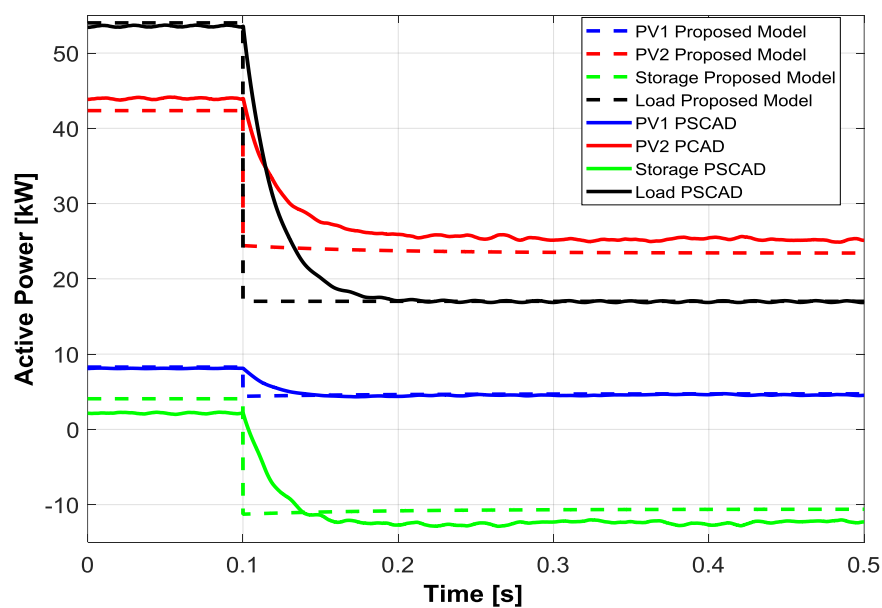


Figure 16. Active power time profile for the load decreasing scenario; the solid line refers to PSCAD model while dashed ones refer to the proposed approach.

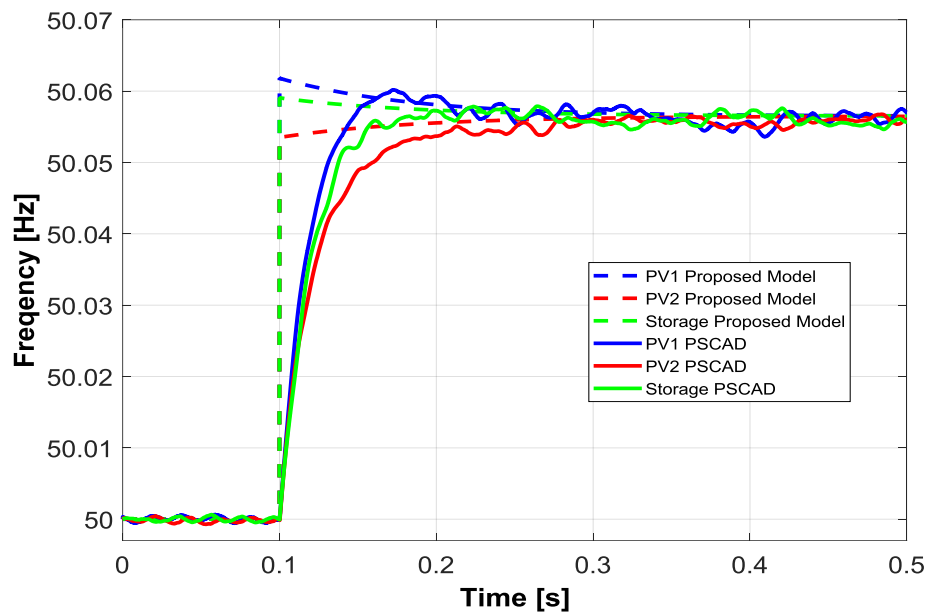


Figure 17. Frequencies output time profile for the load decreasing scenario; the solid line refers to PSCAD model while dashed ones refer to the proposed approach.

Due to the fact that the initial PVs' voltages are over V_{MPP} , (653.4 V and 712.8 V respectively), the decrease of the active power production determines an increase in the DC voltages (Figure 18).

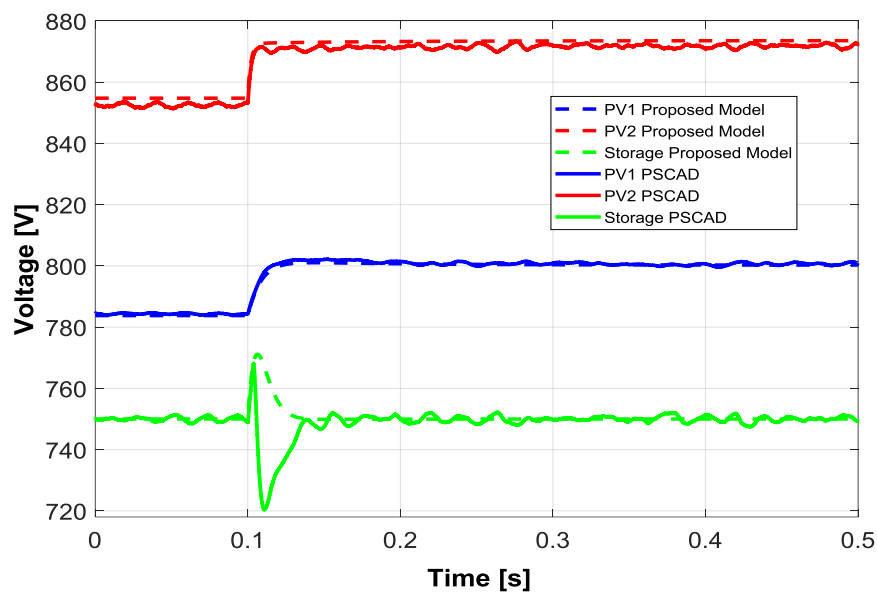


Figure 18. Active power time profile for the load decreasing scenario; the solid line refers to PSCAD model while dashed ones refer to the proposed approach.

The effect of the contingency on the storage system is that it starts absorbing power, which is allowed by a change in the sign of the current. Firstly, this current is absorbed by the DC link storage capacitor; in fact, in Figure 18, an overvoltage transient of about 0.03 s occurs in the proposed model, while an overvoltage transient of about 0.01 s occurs in the complete one. The current behavior is proposed in Figure 19. This different dynamic is due to a discontinuous conduction mode, typical

of DC/DC converters when dealing with low current values [46]. This phenomenon is extinguished when the active power inverts its sign activating the buck converter control.

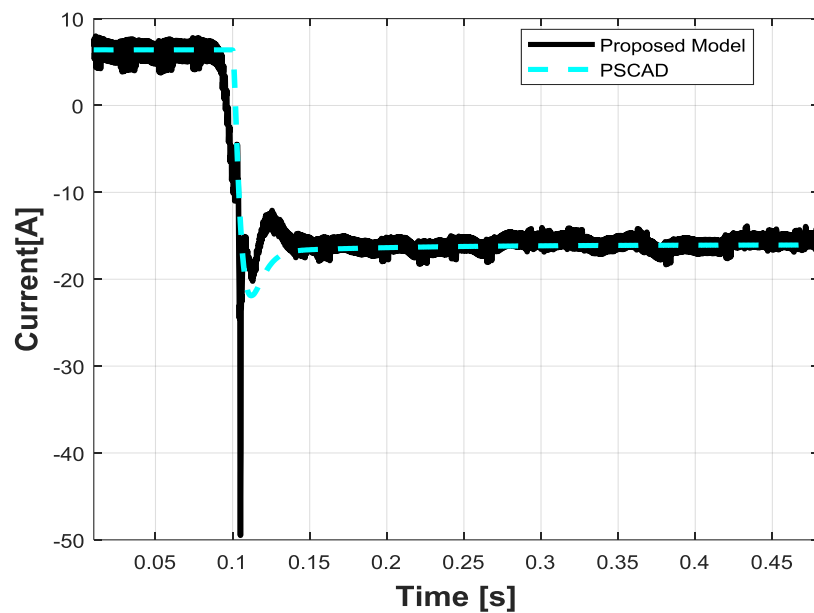


Figure 19. L_{ST} current profile for the load decreasing scenario; the solid line refers to PSCAD model while dashed ones refer to the proposed approach.

Finally, the examination of the voltage at Q2 bus highlights again the good performances of the simplified model and the fact that, after this perturbation, such a voltage still lies inside the feasible range ($\pm 5\%$ of its rated value) (Figure 20).

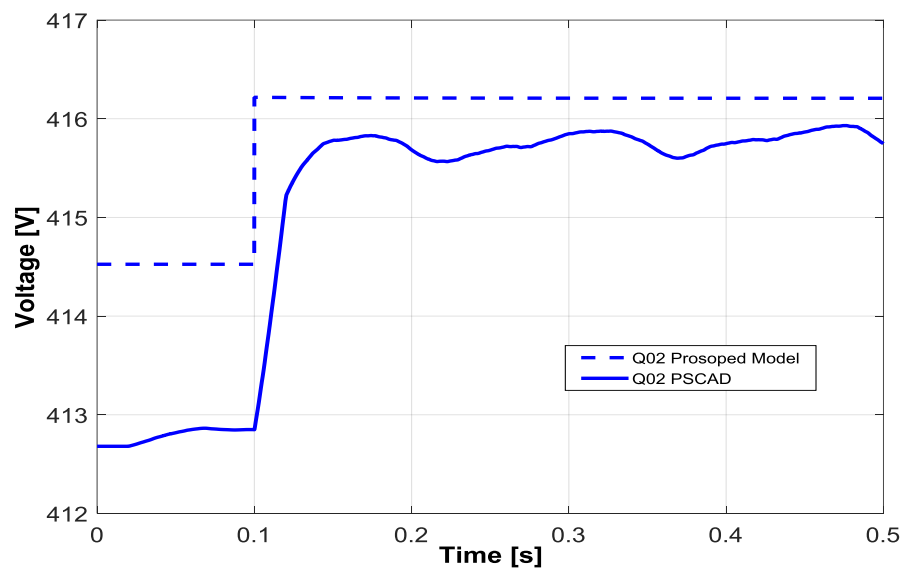


Figure 20. Q2 bus voltage time profile for the load decreasing scenario; the solid line refers to PSCAD model while dashed ones refer to the proposed approach.

6.2. Isochronous Control Simulations

Two simulations performed to verify the performances of the proposed model with the isochronous controller are presented here.

6.2.1. Active Power Increasing Simulation (S3)

The first simulation starts from the initial states appearing in Table 9 and consists of a reduction of the load resistance from 3 to 1.2 Ω (corresponding to 53 and 130 kW) at 0.1 seconds from the beginning of the simulation (again carried out at constant conditions of external temperature and solar radiation).

Table 9. S3—Initial states.

PV1	PV2	Storage	DC/DC Converter
$V_{DC,1} = 659.4$ V	$V_{DC,2} = 712.8$ V	$V_{DC,3} = 750.0$ V	$\chi_1 = 0.093$
$\eta_{11} = 0.2234$	$\eta_{12} = 0.2478$	$I_{ST} = -66.5$ A	$\chi_2 = 0.907$
$\eta_{21} = 1.01$	$\eta_{22} = 0.94$	SOC = 10%	
$\psi_1 = 0$ rad	$\psi_2 = 0$ rad	$\psi_3 = 0$ rad	

The increase of active power is fully provided by the storage, as shown in Figure 21. This implies that the storage current increases to a positive value; firstly, this current is supplied by the DC link storage capacitor causing a voltage dip (Figure 22). The different storage DC voltage dynamic behaviour of the two models shown in Figure 22 is due to a discontinuous conduction mode, typical of DC/DC converters when dealing with low current values [46]. This phenomenon, that can also be noticed in Figure 23, is extinguished when the active power changes its sign and activates the boost converter control. On the other hand, the final working point of the PV units is the same as the pre-contingency one, according to their power control mode.

Performing a comparison, it can be observed that the simplified model is not able to capture the oscillatory transients caused by the perturbation; however, a very good agreement is obtained in the steady-state behavior reproduction.

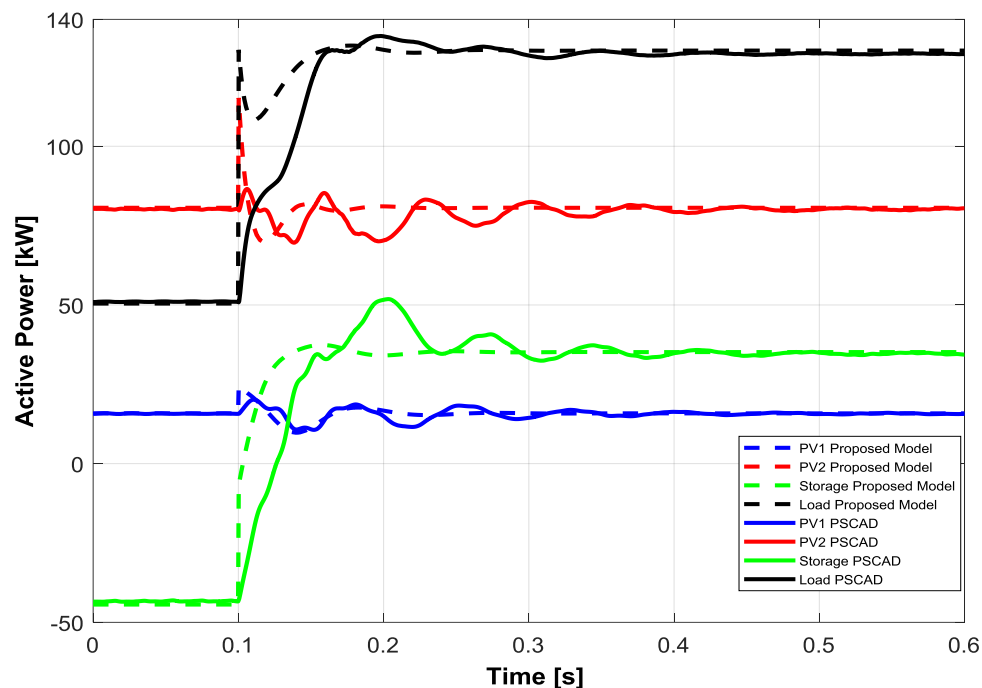


Figure 21. Active power time profile for S3; the solid lines refer to PSCAD model while dashed ones refer to the proposed approach

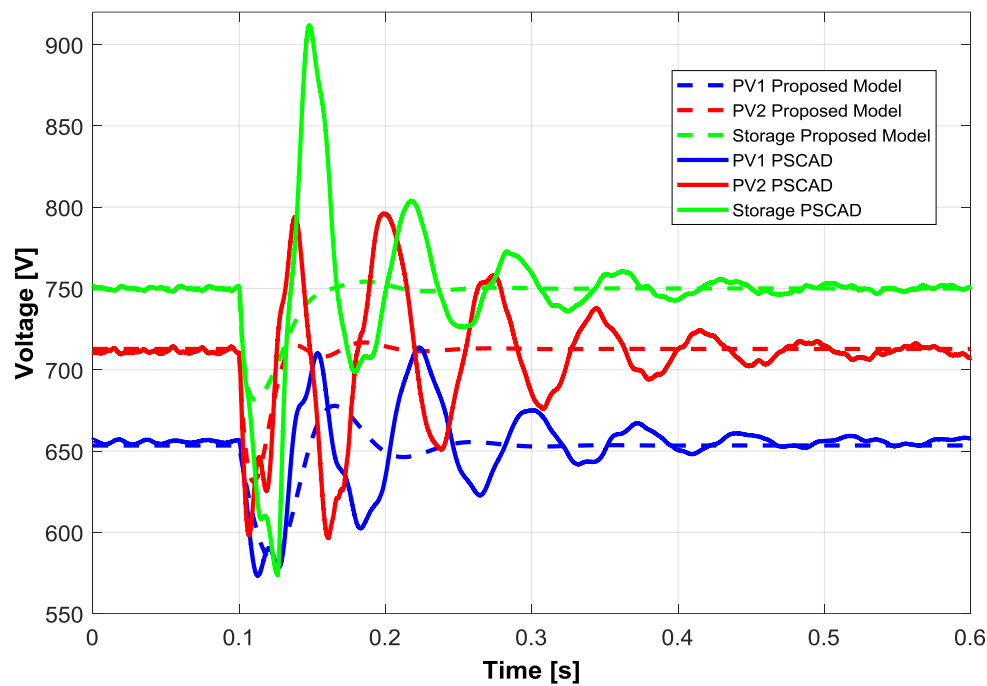


Figure 22. DC capacitor voltage time profile for S3; the solid lines refer to PSCAD model while dashed ones refer to the proposed approach.

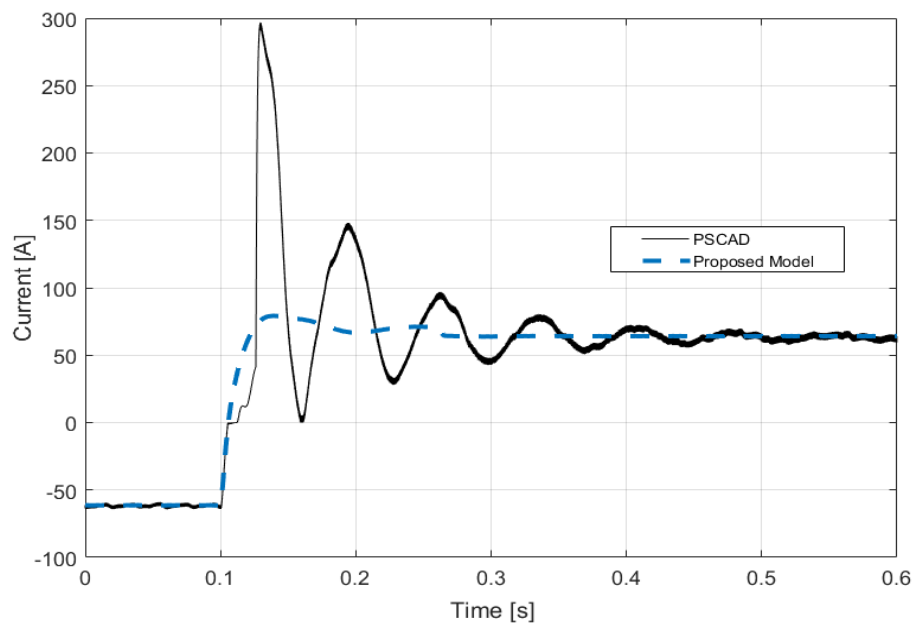


Figure 23. L_{ST} current for S3; the solid lines refer to PSCAD model while dashed ones refer to the proposed approach.

The prediction of the behavior of the voltage at Q2 bus is quite satisfactory (see Figure 24) as the simplified model is able to capture both the initial voltage dip (with a slight underestimation of its amplitude) and the final working point (laying inside the range of $\pm 5\%$ of the rated value).

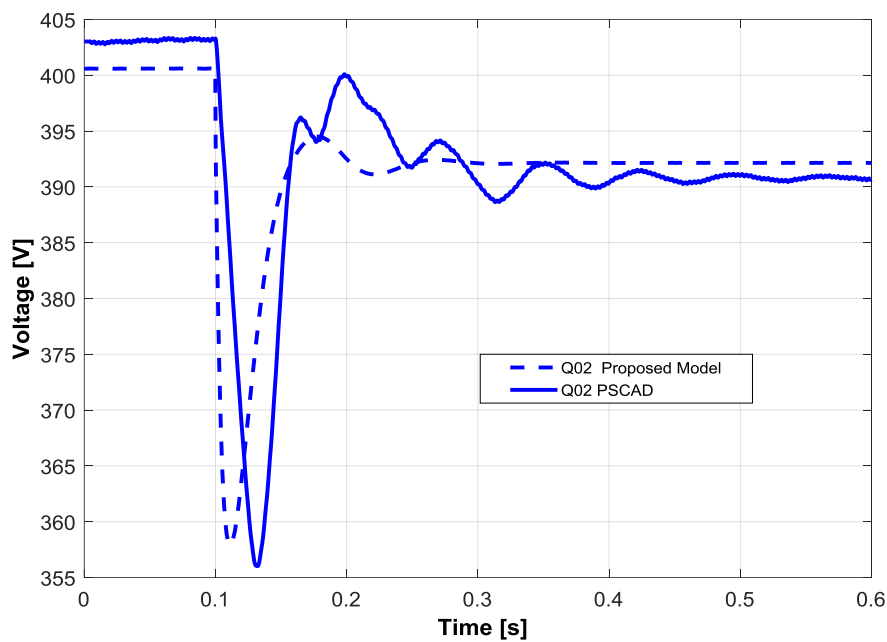


Figure 24. Q2 bus voltage time profile for S3; the solid lines refer to PSCAD model while dashed ones refer to the proposed approach.

6.2.2. Double Perturbation Simulation (S4)

The second simulation concerning the isochronous control logic consists of a double variation in the same scenario. In particular, a load variation and an irradiance decreasing according to two different ramp profiles are presented here. The load variation starts at 0.1 s and consists of a decreasing of the active power absorbed by the load from 39 to 31 kW in 0.1 s, while the decreasing irradiance consists of a halving from 1000 to 500 W/m² in 0.5 s starting at 1.1 s. The initial states of the simulation are provided in Table 10.

Table 10. S4—Initial States.

PV1	PV2	Storage	DC/DC Converter
$V_{DC,1} = 659.4$ V	$V_{DC,2} = 712.8$ V	$V_{DC,3} = 750.0$ V	$\chi_1 = 0.023$
$\eta_{11} = 0.2595$	$\eta_{12} = 0.2889$	$I_{ST} = -72.07$ A	$\chi_2 = 0.977$
$\eta_{21} = 0.99$	$\eta_{22} = 0.90$	SOC = 80%	
$\psi_1 = 0$ rad	$\psi_2 = 0$ rad	$\psi_3 = 0$ rad	

When the ramp variation load occurs, the storage must absorb more active power (Figure 25) in order to guarantee the active power balance. The DC PV and storage voltages and the DC storage current are not affected by this variation, except for a brief transient. This can be ascribed to the fact that a ramp variation causes fewer problems in the dynamic response than a step variation as in the previous simulations. When the irradiance decreases each PV unit supplies less active power (Figure 25) and according to their control mode the DC voltages decrease to the new V_{MPP} (Figure 26).

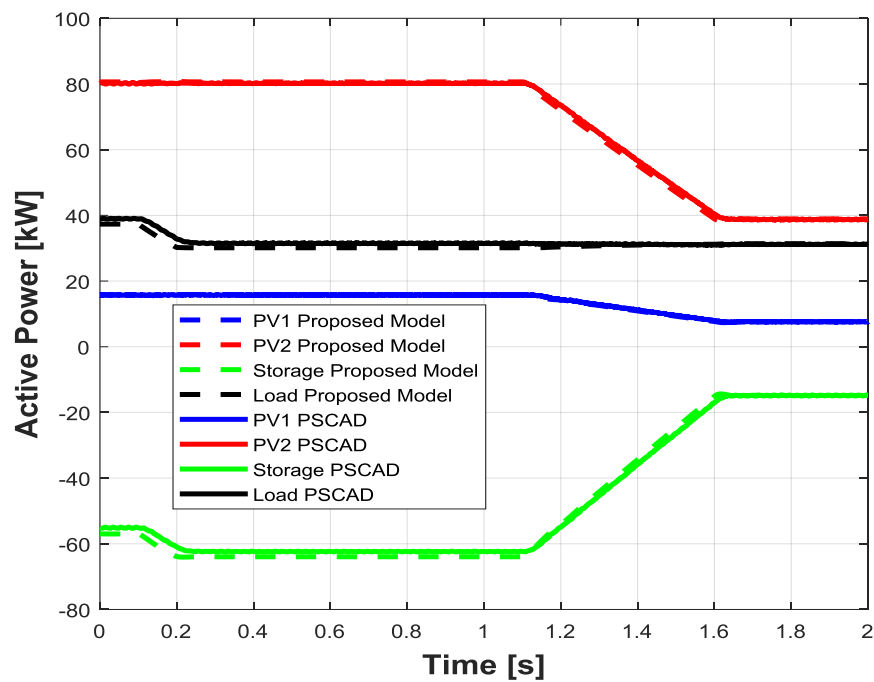


Figure 25. Active power time profile for S4; the solid lines refer to PSCAD model while dashed ones refer to the proposed approach.

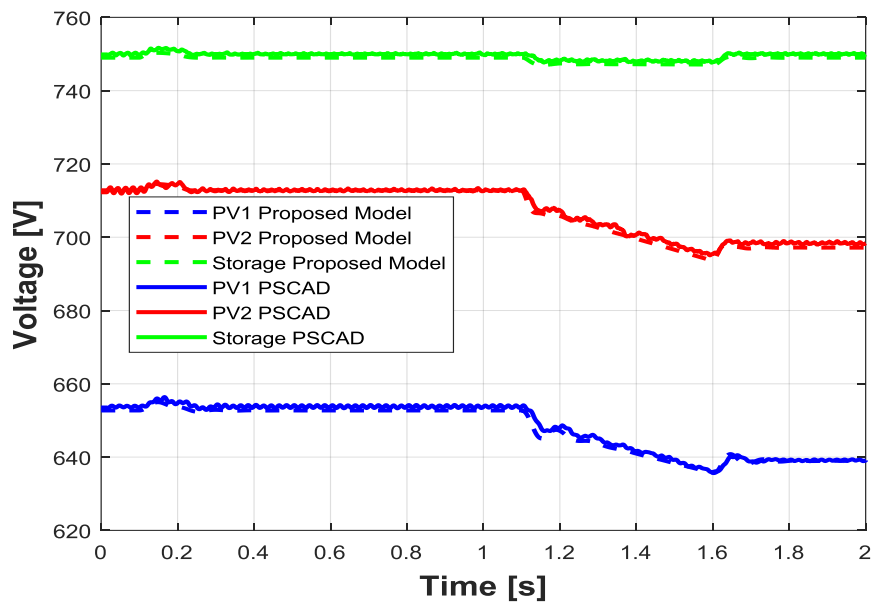


Figure 26. DC capacitor voltage time profile for S4; solid lines refer to PSCAD model while dashed ones refer to the proposed approach.

As can be seen in Figure 27, the Q2 bus voltage is always between the acceptable limits and has some small variations according to the variation described above. Analogue conclusions can be drawn for L_{ST} current, shown in Figure 28.

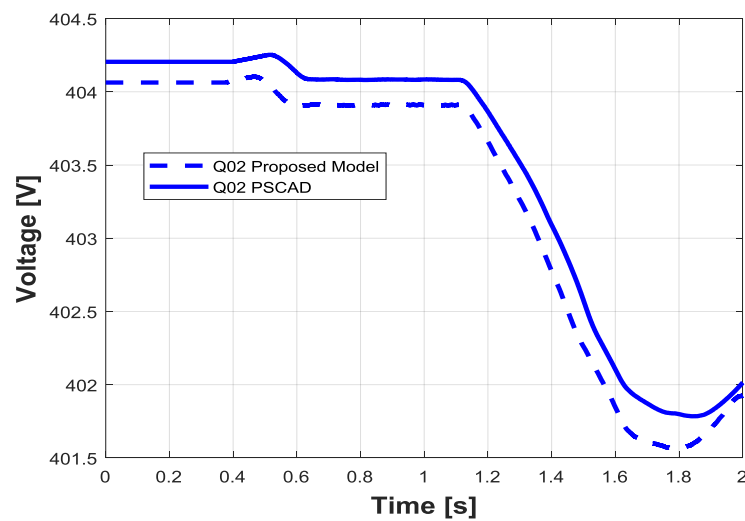


Figure 27. Q2 bus voltage time profile for S4; the solid lines refer to PSCAD model while dashed ones refer to the proposed approach.

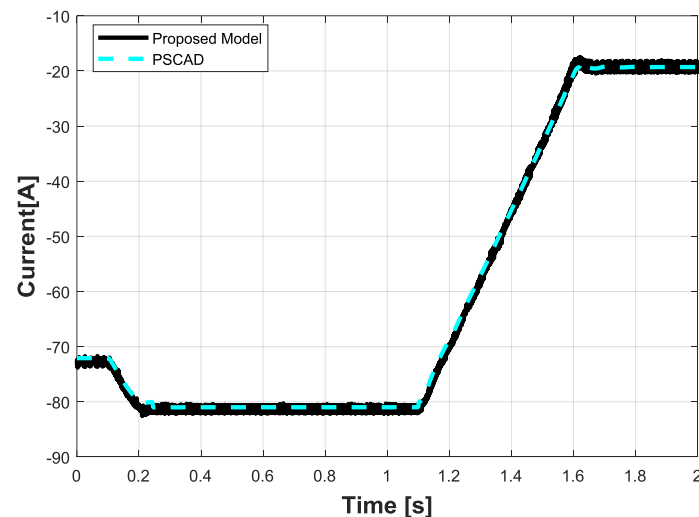


Figure 28. L_{ST} current for S4; the solid lines refer to PSCAD model while dashed ones refer to the proposed approach.

In all the figures presented, the agreement in the dynamic response between the proposed and the PSCAD models is improved with respect to the previous simulations S3. Indeed, the ramp variations affect the dynamic response less than a step variation; thus, what can be concluded is that the smoother is the dynamic variation, the better the agreement between the two models.

7. Conclusions

This paper presented a simplified modelling approach to study the behavior of MGs characterized by all of the generation being interfaced to the AC part of the MG by means of power electronic devices in an islanded configuration. The aim of the article was to define a simplified but effective representation for this kind of MGs, in order to provide a useful and reliable tool for the validation of innovative control strategies for islanded MGs. The proposed model can be described by a system of ordinary differential equations that can be implemented in a general-purpose software with a reduced computational effort. The peculiarity of the proposed methodology is that it is not suited for a specific control strategy or MG structure, but can be adapted and implemented for different control strategies,

topologies and generation mixes. Contrary to other simplified MG models, the proposed model accounts for power losses, voltage drops, DC voltage and frequency dynamics; these are the reasons why it is fit to be used as an environment to implement and test primary frequency and voltage control logics. Moreover, the usefulness of the proposed model is represented by the simulation time-saving with respect to traditional power system simulators and by the possibility to handle the MG dynamics without licensed and specific software. The effectiveness and the good trade-offs of the proposed model have been evaluated by means of a comparison with a detailed representation of a MG test case in the PSCAD-EMTDC environment. In order to account for a realistic test case characterized by known parameters and control logics, the proposed methodology was tested modeling the islanded portion of the SPM of the Savona Campus of Genoa University. This MG can be operated with two different island control strategies; the droop and isochronous strategies. Simulations performed with both the previously mentioned control strategies highlighted the good behavior of the proposed model, particularly if one considers the elements that are relevant with respect to the characterization of the system for a primary frequency and voltage control validation purpose.

Future work will imply the validation of the proposed model against experimental measurements that can be performed in the SPM and the use of the simplified model to develop and assess the performances of more advanced controllers—e.g., an MPC based controller—before their actual implementation in the SPM.

Author Contributions: Marco Invernizzi and Renato Procopio outline the basic theories behind the research work; Massimo Brignone and Andrea Bonfiglio elaborate the system control equations; Alessandro Labella and Daniele Mestriner conceived and designed the experiments, performed the experiments and analyzed the data. All the authors wrote the paper.

Conflicts of Interest: The authors declare no conflict of interest.

Nomenclature

Acronyms

SQ	Switchgear
PV	Photovoltaic source
SPM	Smart Polygeneration Microgrid

Variables

α	Solar irradiation
T	External temperature
SOC	State of charge
δ_k	Angle of the k -th source
φ_k	Phase of the k -th source
ω_k	Angular frequency of the k -th source
m_k	Modulation index of the k -th source
$\dot{V}_{AC,k}$	Voltage phasor of the k -th source
$\dot{I}_{AC,k}$	Current phasor of the k -th source
$V_{DC,k}$	Voltage across the capacitor
I_{ST}	L_{ST} current
E	Storage internal e.m.f.
V_{MPP}	Maximum power point voltage at specified conditions
χ_1	Integrator control output of boost level of DC/DC converter
χ_2	Integrator control output of buck level of DC/DC converter
$\eta_{1,k}$	Integrator control output of active power control of the k -th source
$\eta_{2,k}$	Integrator control output of reactive power control of the k -th source
Y_E	Extended admittance matrix
$G_{i,k}$	Real part of the i - k -th element of Y_E
$B_{i,k}$	Imaginary part of the i - k -th element of Y_E
$V_{DC,k}$	Voltage across the C_k

Constants

R_{int}	Internal resistance of the chemical storage
L_{ST}	Storage side inductance filter of DC/DC converter
C_k	DC capacitor of the k -th inverter
$m_{D,k}$	Active power droop coefficient of the k -th source
$n_{D,k}$	Reactive power droop coefficient of the k -th source
NCC	Storage nominal current capacity

Indices

k	Index of sources; 1 refers to PV1, 2 to PV2, 3 to storage
i	Auxiliary index for k

Functions

f	Function describing ODE system without control
f_D	Function describing ODE system with droop logic
f_I	Function describing ODE system with isochronous logic
g_D	Function describing algebraic equations subsystem with droop logic
g_I	Function describing algebraic equations subsystem with isochronous logic
K_{ST}	Voltage DC/DC converter transfer function

References

1. Hatziargyriou, N.; Asano, H.; Iravani, R.; Marnay, C. Microgrids. *IEEE Power Energy Mag.* **2007**, *5*, 78–94. [CrossRef]
2. Sun, I.; Kim, S. Energy R&D towards Sustainability: A Panel Analysis of Government Budget for Energy R&D in OECD Countries (1974–2012). *Sustainability* **2017**, *9*, 617.
3. Ardito, L.; Procaccianti, G.; Menga, G.; Morisio, M. Smart Grid Technologies in Europe: An Overview. *Energies* **2013**, *6*, 251. [CrossRef]
4. Gonzalez-Longatt, F.M.; Bonfiglio, A.; Procopio, R.; Verduci, B. Evaluation of inertial response controllers for full-rated power converter wind turbine (Type 4). In Proceedings of the IEEE Power and Energy Society General Meeting, Boston, MA, USA, 17–21 July 2016; pp. 1–5.
5. Pichetjamroen, A.; Ise, T. Power Control of Low Frequency AC Transmission Systems Using Cycloconverters with Virtual Synchronous Generator Control. *Energies* **2017**, *10*, 34. [CrossRef]
6. Bonfiglio, A.; Brignone, M.; Delfino, F.; Invernizzi, M.; Pampararo, F.; Procopio, R. A technique for the optimal control and operation of grid-connected photovoltaic production units. In Proceedings of the 2012 47th International Universities Power Engineering Conference, London, UK, 4–7 September 2012; pp. 1–6.
7. Delfino, B.; Fornari, F.; Procopio, R. An effective SSC control scheme for voltage sag compensation. *IEEE Trans. Power Deliv.* **2005**, *20*, 2100–2107. [CrossRef]
8. Fornari, F.; Procopio, R.; Bollen, M.H.J. SSC compensation capability of unbalanced voltage sags. *IEEE Trans. Power Deliv.* **2005**, *20*, 2030–2037. [CrossRef]
9. Manitoba-HVDC. PSCAD Library. Available online: <https://hvdc.ca/knowledge-library/reference-material> (accessed on 23 July 2017).
10. PartSim. SPICE Simulator. Available online: www.partsim.com/simulator (accessed on 23 July 2017).
11. Plexim. PLECS. Available online: <https://www.plexim.com/> (accessed on 23 July 2017).
12. Bendato, I.; Bonfiglio, A.; Brignone, M.; Delfino, F.; Pampararo, F.; Procopio, R. Definition and On-Field Validation of a Microgrid Energy Management System to manage Load and Renewables Uncertainties and System Operator Requirements. *Electric Power Syst. Res. J.* **2017**, *146*, 349–361. [CrossRef]
13. Porsinger, T.; Janik, P.; Leonowicz, Z.; Gono, R. Modelling and Optimization in Microgrids. *Energies* **2017**, *10*, 523. [CrossRef]
14. Aman, S.; Simmhan, Y.; Prasanna, V.K. Energy management systems: State of the art and emerging trends. *IEEE Community Mag.* **2013**, *51*, 114–119. [CrossRef]
15. Lopes, J.A.P.; Moreira, C.L.; Madureira, A.G. Defining control Strategies for Microgrids islanded Operations. *IEEE Trans. Power Syst.* **2006**, *21*, 916–924. [CrossRef]
16. Dall’Anese, E.; Zhu, H.; Giannakis, G.B. Distributed optimal power flow for smart microgrids. *IEEE Trans. Smart Grid* **2013**, *4*, 1464–1475. [CrossRef]

17. Bonfiglio, A.; Delfino, F.; Invernizzi, M.; Labella, A.; Mestriner, D.; Procopio, R.; Serra, P. Approximate characterization of large Photovoltaic power plants at the Point of Interconnection. In Proceedings of the 2015 50th International Universities Power Engineering Conference (UPEC), Stoke-on-Trent, UK, 1–4 September 2015.
18. Muljadi, E.; Butterfield, C.P.; Ellis, A.; Mechenbier, J.; Hochheimer, J.; Young, R.; Miller, N.; Delmerico, R.; Zavadil, R.; Smith, J.C. Equivalencing the collector system of a large wind power plant. In Proceedings of the IEEE Power Engineering Society General Meeting, Montreal, QC, Canada, 18–22 June 2006.
19. Bonfiglio, A.; Delfino, F.; Invernizzi, M.; Serra, P.; Procopio, R. Criteria for the Equivalent Modeling of Large Photovoltaic Power Plants. In Proceedings of the IEEE Power and Energy Society General Meeting, National Harbor, MD, USA, 27–31 July 2014.
20. Changchun, C.; Lihua, D.; Weili, D.; Jianyong, Z. Characteristic model based micro-grid equivalent modeling. In Proceedings of the 2014 International Conference on Power System Technology, Chengdu, China, 20–22 October 2014; pp. 3035–3040.
21. Hussain, A.; Bui, V.H.; Kim, H.M. Robust Optimization-Based Scheduling of Multi-Microgrids Considering Uncertainties. *Energies* **2016**, *9*, 278. [[CrossRef](#)]
22. Ahn, C.; Peng, H. Decentralized and Real-Time Power Dispatch Control for an Islanded Microgrid Supported by Distributed Power Sources. *Energies* **2013**, *6*, 6439. [[CrossRef](#)]
23. Hernandez, L.; Baladrón, C.; Aguiar, J.; Carro, B.; Sanchez-Esguevillas, A.; Lloret, J. Short-Term Load Forecasting for Microgrids Based on Artificial Neural Networks. *Energies* **2013**, *6*, 1385. [[CrossRef](#)]
24. Basak, P.; Saha, A.K.; Chowdhury, S.; Chowdhury, S.P. Microgrid: Control techniques and modeling. In Proceedings of the 2009 44th International Universities Power Engineering Conference (UPEC), Glasgow, UK, 1–4 September 2009; pp. 1–5.
25. Bonfiglio, A.; Barillari, L.; Brignone, M.; Delfino, F.; Pampararo, F.; Procopio, R.; Rossi, M.; Bracco, S.; Robba, M. An optimization algorithm for the operation planning of the University of Genoa smart polygeneration microgrid. In Proceedings of the 2013 IREP Symposium Bulk Power System Dynamics and Control—IX Optimization, Security and Control of the Emerging Power Grid, Rethymno, Greece, 25–30 August 2013.
26. Hou, X.; Sun, Y.; Yuan, W.; Han, H.; Zhong, C.; Guerrero, J. Conventional P- ω /Q-V Droop Control in Highly Resistive Line of Low-Voltage Converter-Based AC Microgrid. *Energies* **2016**, *9*, 943. [[CrossRef](#)]
27. MChandorkar, C.; Divan, D.M.; Adapa, R. Control of parallel connected inverters in standalone AC supply systems. *IEEE Trans. Ind. Appl.* **1993**, *29*, 136–143. [[CrossRef](#)]
28. Labella, A.; Mestriner, D.; Procopio, R.; Brignone, M. A new method to evaluate the stability of a droop controlled micro grid. In Proceedings of the 2017 10th International Symposium on Advanced Topics in Electrical Engineering (ATEE), Bucharest, Romania, 23–25 March 2017; pp. 448–453.
29. Bidram, A.; Davoudi, A. Hierarchical Structure of Microgrids Control System. *IEEE Trans. Smart Grid* **2012**, *3*, 1963–1976. [[CrossRef](#)]
30. Guerrero, J.M.; Loh, P.C.; Lee, T.L.; Chandorkar, M. Advanced Control Architectures for Intelligent Microgrids—Part II. *IEEE Trans. Ind. Electron.* **2013**, *60*, 1263–1270. [[CrossRef](#)]
31. Guerrero, J.M.; Chandorkar, M.; Lee, T.L.; Loh, P.C. Advanced control architectures for intelligent microgrids—Part I: Decentralized and hierarchical control. *IEEE Trans. Ind. Electron.* **2013**, *60*, 1254–1262. [[CrossRef](#)]
32. Su, X.; Han, M.; Guerrero, J.; Sun, H. Microgrid Stability Controller Based on Adaptive Robust Total SMC. *Energies* **2015**, *8*, 1784. [[CrossRef](#)]
33. Chlela, M.; Mascarella, D.; Joos, G.; Kassouf, M. Fallback Control for Isochronous Energy Storage Systems in Autonomous Microgrids Under Denial-of-Service Cyber-Attacks. *IEEE Trans. Smart Grid* **2017**, *PP*, 1. [[CrossRef](#)]
34. Xiao, S.; Yim-Shu, L.; Dehong, X. Modeling, analysis, and implementation of parallel multi-inverter systems with instantaneous average-current-sharing scheme. *IEEE Trans. Power Electron.* **2003**, *18*, 844–856. [[CrossRef](#)]
35. Parisio, A.; Rikos, E.; Glielmo, L. A Model Predictive Control Approach to Microgrid Operation Optimization. *IEEE Trans. Control Syst. Technol.* **2014**, *22*, 1813–1827. [[CrossRef](#)]
36. Nguyen, T.T.; Yoo, H.J.; Kim, H.M. Analyzing the Impacts of System Parameters on MPC-Based Frequency Control for a Stand-Alone Microgrid. *Energies* **2017**, *10*, 417. [[CrossRef](#)]

37. Kerdphol, T.; Rahman, F.; Mitani, Y.; Hongesombut, K.; Küfeoğlu, S. Virtual Inertia Control-Based Model Predictive Control for Microgrid Frequency Stabilization Considering High Renewable Energy Integration. *Sustainability* **2017**, *9*, 773. [CrossRef]
38. Bonfiglio, A.; Delfino, F.; Invernizzi, M.; Perfumo, A.; Procopio, R. A feedback linearization scheme for the control of synchronous generators. *Electric Power Compon. Syst.* **2012**, *40*, 1842–1869. [CrossRef]
39. Bonfiglio, A.; Delfino, F.; Pampararo, F.; Procopio, R.; Rossi, M.; Barillari, L. The Smart Polygeneration Microgrid test-bed facility of Genoa University. In Proceedings of the 47th International Universities Power Engineering Conference, London, UK, 4–7 September 2012.
40. Bell, K.R.W.; Tleis, A.N.D. Test system requirements for modelling future power systems. In Proceedings of the 2010 IEEE Power and Energy Society General Meeting, Providence, RI, USA, 25–29 July 2010; pp. 1–8.
41. Böke, U. A simple model of photovoltaic module electric characteristics. In Proceedings of the European Conference on Power Electronics and Applications, Aalborg, Denmark, 2–5 September 2007.
42. FIAMM. SoNick ST523. Available online: [Fiamm.com/media/20150209-st523_datasheet.pdf](http://fiamm.com/media/20150209-st523_datasheet.pdf) (accessed on 21 July 2017).
43. Rexed, I.; Behm, M.; Lindbergh, G. Modelling of ZEBRA Batteries; Royal Institute of Technology. Available online: https://www.kth.se/polopoly_fs/1.187945!/Menu/general/column-content/attachment/59.pdf (accessed on 21 July 2017).
44. Sudworth, J.L. Zebra batteries. *J. Power Sources* **1994**, *51*, 105–114. [CrossRef]
45. Seyedmahmoudian, M.; Mekhilef, S.; Rahmani, R.; Yusof, R.; Renani, E. Analytical Modeling of Partially Shaded Photovoltaic Systems. *Energies* **2013**, *6*, 128. [CrossRef]
46. Erickson, R.; Maksimovic, D. *Fundamentals of Power Electronics*, 2nd ed.; Springer US: London, UK, 2004; pp. 1–883.
47. Kundur, P.; Balu, N.J.; Lauby, M.G. *Power System Stability and Control*; McGraw-Hill: Palo Alto, CA, USA, 1994; pp. 1–1200.
48. Guerrero, J.M.; Vasquez, J.C.; Matas, J.; Vicuna, L.G.; Castilla, M. Hierarchical Control of Droop-Controlled AC and DC Microgrids—A General Approach toward Standardization. *IEEE Trans. Ind. Electron.* **2011**, *58*, 158–172. [CrossRef]
49. Simpson-Porco, J.W.; Dörfler, F.; Bullo, F. Synchronization and power sharing for droop-controlled inverters in islanded microgrids. *Automatica* **2013**, *49*, 2603–2611. [CrossRef]
50. Mohd, A.; Ortjohann, E.; Sinsukthavorn, W.; Lingemann, M.; Hamsic, N.; Morton, D. Isochronous load sharing and control for inverter-based distributed generation. In Proceedings of the 2009 International Conference on Clean Electrical Power, Capri, Italy, 9–11 June 2009; pp. 324–329.
51. Kim, J.Y.; Jeon, J.H.; Kim, S.K.; Cho, C.; Park, J.H.; Kim, H.M.; Nam, K. Cooperative Control Strategy of Energy Storage System and Microsources for Stabilizing the Microgrid during Islanded Operation. *IEEE Trans. Power Electron.* **2010**, *25*, 3037–3048.
52. Milano, F. Power system modelling and scripting. In *Power Systems*; Springer: London, UK, 2010; Volume 54, pp. 1–550.
53. Delfino, F.; Procopio, R.; Rossi, M.; Ronda, G. Integration of large-size photovoltaic systems into the distribution grids: A P-Q chart approach to assess reactive support capability. *IET Renew. Power Gener.* **2010**, *4*, 329–340. [CrossRef]

